

# Ultrafast Organic Emulsion-Based Synthesis of High-Performance Cathode Materials for Rechargeable Batteries

Francisco J. Garcia-Garcia, Saúl Rubio, Xiaoqiong Du, Xuyun Guo, Julio E. de la Rosa-Melian, Eva M. Pérez-Soriano, Cristina Arévalo, Isabel Montealegre-Meléndez, Ana M. Beltrán, Valeria Nicolosi, and Juan G. Lozano\*

In this work, an emulsion-based organic synthesis route for the fabrication of cathode materials for rechargeable batteries, which drastically reduces the synthesis time, is presented. In particular, it decreases the times necessary to obtain the preheat-treatment mixture of oxides down to 4 min, markedly faster than the typical times ranging from 90 to 120 min necessary by solid-state reaction-based techniques to several hours required in the more

conventional sol-gel routes. In all cases, the resulting products closely resemble those obtained via other established but more time-consuming synthesis methods. They demonstrate superior electrochemical properties, amongst the best results reported so far in the literature. Furthermore, the proposed route also saves energy, is cost-effective, nontoxic, and highly scalable, making it attractive for greener industrial application.

## 1. Introduction

Climate change and the decreasing availability of fossil fuels require society to move towards sustainable and renewable resources. Most renewable sources are inherently intermittent, and therefore, it is imperative to seek efficient energy storage systems that can store the electricity generated and release it on demand. Similarly, in order to transfer to a low-carbon economy not reliant on fossil fuels, it is necessary to achieve a full electrification of transport. In this context, rechargeable batteries—particularly lithium-ion batteries (LIBs) and sodium-ion batteries

(SIBs)—play a crucial role. LIBs have revolutionized portable electronics and play an increasingly important role in electric vehicles. SIBs are a cheaper alternative to LIBs due to the abundance of sodium and are therefore suitable for large-scale storage.

There are a number of promising candidate materials systems for both LIBs and SIBs battery cathodes that theoretically allow further storage improvements or have some significant advantages. Amongst those, olivine, or tavorite structures, lithium-rich layered oxides, nickel-rich layered oxides, or spinel structures for LIBs and transition metal oxides, NASICON, or Prussian blue for SIBs can be highlighted.

Alongside the development of new, more efficient and more environmentally friendly cathode materials for emerging LIBs and SIBs, the improvement of current synthesis techniques is also a must, although often overlooked. Existing synthesis routes for the fabrication of cathode materials for rechargeable batteries have important limitations in terms of efficiency, cost, scalability, time, or energy consumption, which have a direct impact on the feasibility of using them at an industrial level.

Most commercial cathodes for LIBs, namely  $\text{LiCoO}_2$  cathodes, and for SIBs at the laboratory level, are synthesized via solid-state reactions of oxide precursors, usually in the form of powders, in a process often referred to as mechanochemistry or mechanosynthesis.<sup>[1–4]</sup> Apart from the solid-state reaction-based techniques, there are other synthesis routes for the fabrication of cathodes for LIBs or SIBs which involve coprecipitation,<sup>[5–10]</sup> hydrothermal,<sup>[11–14]</sup> or sol-gel<sup>[2,15–19]</sup> methods.

Although comparatively less used, emulsion-based synthesis routes are particularly interesting since they offer an efficient approach to achieving better control over the morphology of the material.<sup>[20]</sup> Thermodynamically stable microemulsions consist of a blend of hydrophilic and hydrophobic fluids, with surfactants stabilizing the system to create a thermodynamically stable and isotropic dispersion. When the hydrophobic phase

F. J. Garcia-Garcia, S. Rubio, I. Montealegre-Meléndez, A. M. Beltrán  
Departamento de Ingeniería y Ciencia de los Materiales y del Transporte  
Escuela Politécnica Superior/CATEPS  
Universidad de Sevilla  
41011 Sevilla, Spain

X. Du, X. Guo, V. Nicolosi  
School of Chemistry  
Centre for Research on Adaptive Nanostructures and Nanodevices (CRANN) and Advanced Materials Bio-Engineering Research Centre (AMBER)  
Trinity College Dublin  
Dublin 2, Ireland

J. E. de la Rosa-Melian, E. M. Pérez-Soriano, C. Arévalo, J. G. Lozano  
Departamento de Ingeniería y Ciencia de los Materiales y del Transporte  
Escuela Técnica Superior de Ingeniería  
Universidad de Sevilla  
41092 Sevilla, Spain  
E-mail: jl.suarez@us.es

 Supporting information for this article is available on the WWW under <https://doi.org/10.1002/batt.202500213>

 © 2025 The Author(s). *Batteries & Supercaps* published by Wiley-VCH GmbH. This is an open access article under the terms of the Creative Commons Attribution-NonCommercial License, which permits use, distribution and reproduction in any medium, provided the original work is properly cited and is not used for commercial purposes.

predominates, the hydrophilic liquid is enclosed within surfactant layers, forming reverse micelles. These nanostructures act as miniature reaction vessels, enabling the synthesis of a wide range of nanoparticles. In this sense, emulsion-based techniques have been used to fabricate cathode materials for LIBs, such as  $\text{LiFe}_x\text{Mn}_{2-x}\text{O}_4$ ,<sup>[21]</sup>  $\text{LiMn}_2\text{O}_4$ ,<sup>[22,23]</sup>  $\text{LiNi}_{0.8}\text{Co}_{0.2}\text{O}_2$ ,<sup>[24]</sup> or  $\text{LiCo}_{1/3}\text{Ni}_{1/3}\text{Mn}_{1/3}\text{O}_2$ <sup>[25]</sup> or porous carbon for anodes.<sup>[26]</sup>

In all cases, the resulting products obtained from mixing, coprecipitation, hydrothermal, emulsion or sol-gel routes are further heat-treated to the temperature and time established in the bibliography, depending on the final product to be synthesized.

However, all of these described methods require extended times to obtain the mixture of oxides, which will be heat treated to produce the desired crystalline structure. Besides, none of them are easily scalable to an industrial level. In solid-state reaction mechanical alloying processes, ball-milling times range typically from 90 min to several hours.<sup>[1,4,27]</sup> Besides, the volume of mixture that can be produced is restricted by the volume of the milling jars, and the required equipment—planetary ball mills, normally—has a high economic cost. For the coprecipitation, hydrothermal, sol-gel, or emulsion-based methods reported in the bibliography, the required times to obtain the preheat-treatment products can be as long as 24 h, including mixing times and solvent evaporation<sup>[21–25,27–30]</sup> and the volumes that can be produced are relatively small.

In this work, we present an ultrafast and scalable emulsion-based synthesis route for the fabrication of cathode materials for the next generation of LIBs and SIBs. As test materials,  $\text{Li}_{1.2}\text{Ni}_{0.2}\text{Mn}_{0.6}\text{O}_2$  and  $\text{Na}_{0.66}\text{Ni}_{0.27}\text{Mg}_{0.06}\text{Mn}_{0.66}\text{O}_2$  have been selected, due to their technological relevance and because there are several articles in the bibliography on the synthesis of these materials using alternative synthesis routes which can be employed as a comparison to validate this route.<sup>[28,31–43]</sup> Amongst other advantages, the proposed synthesis technique allows for a drastic reduction of the time required for obtaining the preheat-treatment product down to 4 min and is also very easily scalable. It is a modified version on an organic synthesis route proposed by García-García et al.<sup>[20]</sup> The method, summarized in Figure 1, involves mixing stoichiometric amounts of the metal acetates in water and the use of a nonpolar organic liquid that is not miscible with water. Here, vaseline oil was specifically chosen as it has no known health concerns compared with industrial mineral oils. However, since the ionic metals utilized for the fabrication of the cathodes exhibit a hydrophilic nature, it is necessary to dissolve them in the organic liquid with the assistance

of a surfactant, such as oleic acid. Given the amphiphatic character of oleic acid, upon mixing under the right conditions, inverse micelles will be formed. In these micelles, the nonpolar ends preferentially orient themselves towards the exterior, while the polar end points towards the interior of the micelle, thus encapsulating the water containing the metal ions in solution. These micelles are the basis of an emulsion, which can be further heat-treated to remove the water and the organic anions, and finally, to obtain the final product.

In order to obtain the emulsion, here we have used a shear mixer operating at 15,000 rpm, with the related saving in terms of time—only 4 min until the emulsion has the required consistency—and energy consumption. Additionally, this modified synthetic route has several significant advantages: 1) since it is an emulsion-based procedure, it allows obtaining particles with a controlled morphology and homogeneous size distribution;<sup>[44,45]</sup> 2) one of its most crucial benefits is the use of organic precursors, which leads to the production of noncontaminating reaction side-products; and 3) it holds a broad potential for upscaling to industrial levels, since it would only require resizing the shear mixer and the vessels.

## 2. Results and Discussion

### 2.1. Synthesized $\text{Li}_{1.2}\text{Ni}_{0.2}\text{Mn}_{0.6}\text{O}_2$

Regarding the synthesized  $\text{Li}_{1.2}\text{Ni}_{0.2}\text{Mn}_{0.6}\text{O}_2$ , X-ray diffraction (XRD) patterns display reflections mainly corresponding to the  $\text{Li}_2\text{MnO}_3$ -type monoclinic phase, space group  $C2/m$ , of  $\text{Li}_{1.2}\text{Ni}_{0.2}\text{Mn}_{0.6}\text{O}_2$ . Figure 2a displays the in situ evolution of phases as a function of temperature for the  $\text{Li}_{1.2}\text{Ni}_{0.2}\text{Mn}_{0.6}\text{O}_2$  sample. At room temperature (RT, i.e., after heating at 450 °C for calcination and subsequently cooling), the corresponding XRD pattern displays broad and, comparatively, less intense reflections, which would agree with the formation of a mixture of oxides with very small crystal size randomly oriented. However, the reflections corresponding to the monoclinic phase of  $\text{Li}_{1.2}\text{Ni}_{0.2}\text{Mn}_{0.6}\text{O}_2$  are already clearly identifiable, indicating that even at temperatures as low as 450 °C, small crystallites of the sought-after phase have been formed.

As the temperature increases during the in situ experiment, the reflections corresponding to the monoclinic phase become steadily sharper and more intense, and after cooling back to room temperature, only reflections corresponding to the  $C2/m$  phase

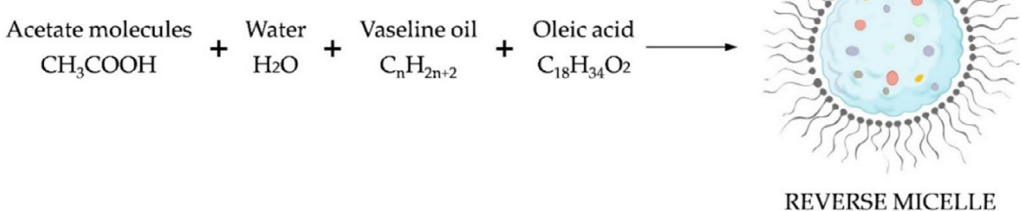
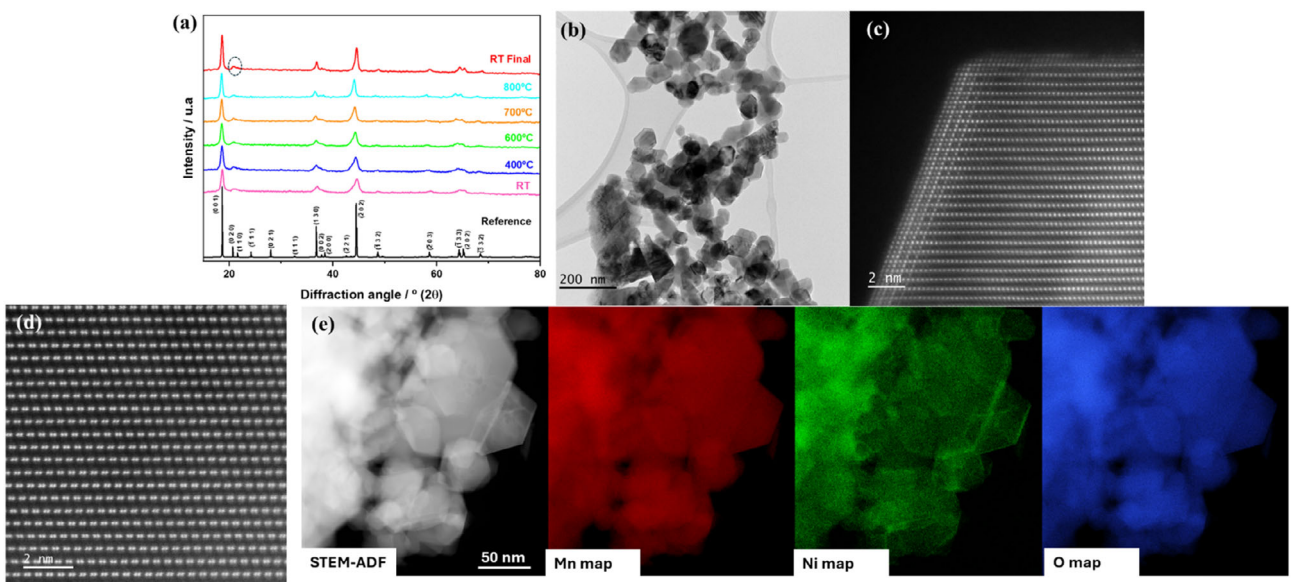


Figure 1. Schematics of the formation of micelles from organic precursors using the proposed route.



**Figure 2.** a) In situ XRD spectra of the  $\text{Li}_{1.2}\text{Ni}_{0.2}\text{Mn}_{0.6}\text{O}_2$  samples taken at room temperature (RT), 400, 600, 700, and 800 °C and after cooling back to room temperature inside the chamber (RT-Final) for the samples synthesized using the proposed organic route and the simulated pattern using a  $\text{C}2/\text{m}$  structure (bottom). The dashed circle indicates the peaks in the 26–36° range commonly identified as the Li-rich phase superstructure; b) conventional TEM micrograph of the synthesized particles; c) HR-STEM image of one of the particles along the [010] direction; and d) the [110] direction showing the dumbbells unequivocally attributed to the  $\text{C}2/\text{m}$  phase. e) ADF-STEM and EDX elemental maps of Mn, Ni, and O showing the elemental distribution with the  $\text{Li}_{1.2}\text{Ni}_{0.2}\text{Mn}_{0.6}\text{O}_2$  particles.

are observed. The peaks in the 26–36° range are commonly identified as the Li-rich phase superstructure (dashed circle in Figure 2a), while the broadening of those peaks is associated with the reported interlayer rotation that limits long-range order.<sup>[38,46]</sup>

Conventional transmission electron microscopy (TEM) was used to elucidate the size and morphology of individual  $\text{Li}_{1.2}\text{Ni}_{0.2}\text{Mn}_{0.6}\text{O}_2$  particles, as well as the particle size distribution in the samples. As can be seen in Figure 2b, the synthesis led to particles displaying an elongated polyhedron shape with some prominently wide and flat facets and an estimated average size (long axis) of  $85 \pm 30$  nm. This is a remarkable result, since the proposed organic route produces both particle size and size distribution very similar to those obtained by sol-gel routes while significantly reducing the synthesis time. Sol-gel routes are often used at a laboratory level since they produce a very good control over particle size, although the associated time consumption does not make it a feasible route for up-scaling.

In order to corroborate the results obtained by XRD and evaluate the crystalline structure and quality of individual  $\text{Li}_{1.2}\text{Ni}_{0.2}\text{Mn}_{0.6}\text{O}_2$  particles, aberration-corrected high-resolution scanning-TEM (STEM) was performed on the samples. As can be seen in Figure 2c, the micrographs taken along the [010] zone axis show the laminar structure characteristic of the Li-rich oxides in both cases, which could be attributed to the monoclinic phase ( $\text{Li}_2\text{MnO}_3$ ) or to the trigonal phase ( $\text{LiMO}_2$ ,  $M$  = transition metals present in the compound). To unambiguously determine the crystalline structure of the particles, further micrographs were taken along the [110] zone axis (Figure 2d). These display a characteristic “dumbbell” structure formed by pairs of transition metal atoms, which is a feature unique to the monoclinic phase and not possible to obtain in any orientation of the trigonal phase.<sup>[46]</sup> Therefore, it can be concluded that the

particles are made of single or multiple grains of a single phase, i.e., monoclinic phase with space group  $\text{C}2/\text{m}$ . Additionally, the images taken along the [010] zone axis (Figure 2c) show that the surfaces of the particles have a 1–2 nm thick layer with brighter contrast and hexagonal patterns on certain facets. This is in good agreement with previous results published in the literature,<sup>[46]</sup> which describe the formation of a nickel-rich thin layer with spinel structure, and an orientation relationship  $(100)_M \parallel (110)_S$ .

The evaluation of the homogeneity of the elemental distribution within the  $\text{Li}_{1.2}\text{Ni}_{0.2}\text{Mn}_{0.6}\text{O}_2$  particles was performed by energy-dispersive X-ray spectroscopy (EDX) mapping in STEM mode, and the results are summarized in Figure 2d. As can be observed, Mn and O have a highly uniform distribution. Within the bulk of the particles, Ni is also homogeneously distributed; however, it tends to diffuse more towards the defects in the particles, particularly the grain boundaries and the particle surface, resulting in the formation of the aforementioned thin spinel layer.

**Figure 3a** shows the first charge and discharge, and capacity retention profiles of lithium half cells assembled with the synthesized  $\text{Li}_{1.2}\text{Ni}_{0.2}\text{Mn}_{0.6}\text{O}_2$  samples, between 2 and 4.8 V, recorded at  $50 \text{ mA g}^{-1}$  (charge–discharge curves corresponding to the 10th, 50th, and 100th cycles, and the corresponding  $dQ/dV$  curves can be found in the Supporting Information (SI), Figure S1). The initial charge and discharge curves of  $\text{Li}_{1.2}\text{Ni}_{0.2}\text{Mn}_{0.6}\text{O}_2$  show a typical initial charge curve of the Li-rich cathode, comprising of a slope between 3.7 and 4.5 V, and a subsequent plateau region at  $\approx 4.8$  V. While the capacity up to 4.5 V can be attributed to the extraction of Li and oxidation of Ni (i.e., from  $\text{Ni}^{2+}$  to  $\text{Ni}^{4+}$ ), the extra capacity observed at 4.8 V is due to oxygen redox reactions of the oxygen sublattice.<sup>[36,39]</sup> This agrees with the cyclic voltammetry (CV) curve shown in Figure 3b of the  $\text{Li}_{1.2}\text{Ni}_{0.2}\text{Mn}_{0.6}\text{O}_2$

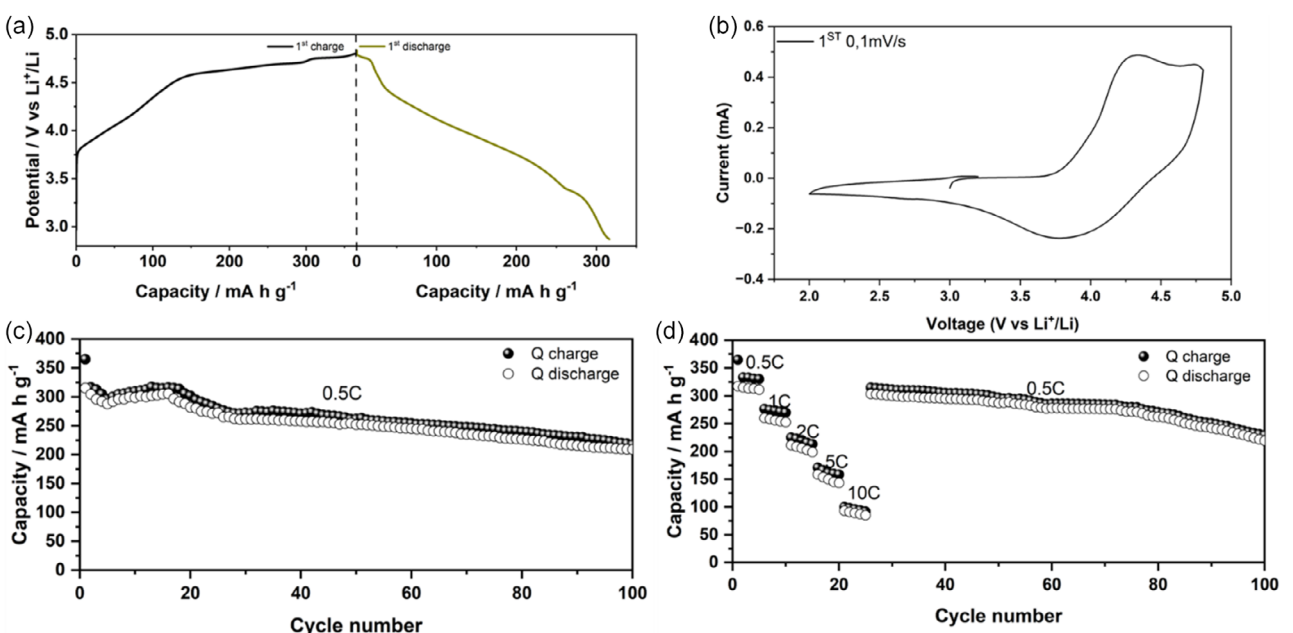


**Figure 3.** a) Galvanostatic first charge/discharge curve. b) CV curve of the  $\text{Li}_{1.2}\text{Ni}_{0.2}\text{Mn}_{0.6}\text{O}_2$  sample, recorded using a scan rate of  $0.1 \text{ mV s}^{-1}$ . c) Retention capacity profiles of the  $\text{Li}_{1.2}\text{Ni}_{0.2}\text{Mn}_{0.6}\text{O}_2$  sample during the first 100 cycles. d) Rate performance of  $\text{Li}_{1.2}\text{Ni}_{0.2}\text{Mn}_{0.6}\text{O}_2$  at room temperature.

sample, recorded using a scan rate of  $0.1 \text{ mV s}^{-1}$  versus  $\text{Li}^+/\text{Li}$ . Apart from the oxidation peak at  $\approx 4.4 \text{ V}$ , which is assigned to  $\text{Ni}^{2+/4+}$  redox followed by oxygen loss, a reduction peak is observed at  $\approx 3.7 \text{ V}$ , attributed to the reduction of  $\text{Ni}^{4+/2+}$ .

The initial charge and discharge capacities of this sample are 364 and  $314 \text{ mA h g}^{-1}$  respectively. The charge and discharge capacity of the sample reaches a stable plateau from the sixth cycle, and after 100 cycles, the charge and discharge capacities are 214 and  $206 \text{ mA h g}^{-1}$ , as shown in Figure 3c which highlights the good electrochemical behavior of samples fabricated through the route presented in this work. The coulombic efficiency after 100 cycles and the rate performance reported for the material synthesized (Figure 3d) using our proposed synthesis route are comparable to some of the best results in the literature for this class of Li-rich materials.<sup>[38,47–50]</sup> Additionally, and for comparison, a sample of  $\text{Li}_{1.2}\text{Ni}_{0.2}\text{Mn}_{0.6}\text{O}_2$  was synthesized using a conventional sol-gel method (see the Supporting Information for details about the synthesis and electrochemical characterization). The first charge capacity and the charge capacity after 100 cycles of the sample synthesized using the proposed organic route are 47 and 27% higher, respectively, as can be concluded by comparing the data presented in (Figure 3 and S3, Supporting Information).

Despite the excellent capabilities of the synthesized material, Figure 3c shows that there is a significant capacity loss after the first charge–discharge cycle, followed by a slower but progressive loss with subsequent cycles. The capacity loss mechanisms are mostly related to structural rearrangement at the atomic scale during charge–discharge cycles. Trapping of metal cations in the interstitial tetrahedral sites or formation of other phases, including spinel, rock salt, or  $\text{Mn}_3\text{O}_4$ -like structures linked to oxygen loss, has been reported.<sup>[51–53]</sup>

To monitor structural changes during cycling, further high-resolution STEM measurements were performed on  $\text{Li}_{1.2}\text{Ni}_{0.2}\text{Mn}_{0.6}\text{O}_2$

particles after one cycle, and after 100 charge–discharge cycles. The results, summarized in Figure 4, indicate that after the first discharge, a very thin ( $\approx 1 \text{ nm}$ ) surface layer of a rock-salt-type structure has formed. A higher contrast is also observed in the alkali metal layer, indicating a partial migration of transition metal atoms, as well as a partial rearrangement of the TMO layer, which would explain the drop in capacity after the first cycle. However, the  $\text{C}2/m$  structure is mostly preserved, which is consistent with the high capacity values measured.

Figure 4b shows an HR-STEM image of the same sample after 100 charge–discharge cycles. It can be observed that, while the layered structure is maintained, the thickness of the spinel/rock-salt structure layer has evolved, reaching a thickness of about 3–4 nm. The progressive growth of this layer would explain the small but gradual capacity loss observed.

## 2.2. Synthesized $\text{Na}_{0.66}\text{Ni}_{0.27}\text{Mg}_{0.06}\text{Mn}_{0.66}\text{O}_2$

Regarding the synthesis of  $\text{Na}_{0.66}\text{Ni}_{0.27}\text{Mg}_{0.06}\text{Mn}_{0.66}\text{O}_2$  particles, the results of the in situ XRD (Figure 5a) show that, globally, as the temperature increases, the reflections mainly correspond to the stable high-temperature  $\text{O}3$  phase, whereas after cooling, the room-temperature stable hexagonal  $\text{P}2$  phase is the predominant. SE-SEM was first used to inspect the topography of the fabricated  $\text{Na}_{0.66}\text{Ni}_{0.27}\text{Mg}_{0.06}\text{Mn}_{0.66}\text{O}_2$  particles. It can be seen (Figure 5b) that most of the particles have a flat hexagonal pyramid-like shape with edges containing steps due to this laminar structure. An analysis of the particle size distribution, estimated by measuring the largest length of each particle of a SE-SEM image, gives an average length of  $2.6 \pm 0.5 \mu\text{m}$ . Aberration-corrected high-resolution STEM results, displayed in Figure 5c, further agree with the formation of the layered  $\text{P}2$  phase. EDX mapping (Figure 5d) proves an excellent homogeneous distribution of all the elements in the sample.

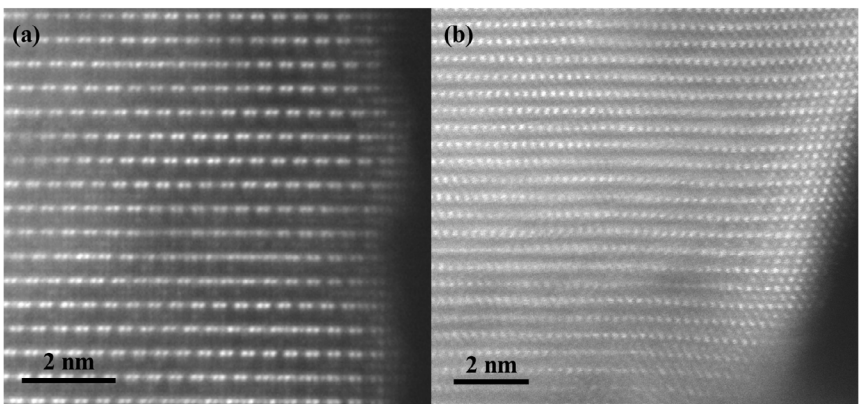


**Figure 4.** HR-STEM micrographs of the  $\text{Li}_{1.2}\text{Ni}_{0.2}\text{Mn}_{0.6}\text{O}_2$  a) after 1 charge–discharge cycle ([100] direction) and b) after 100 cycles ([010] direction).

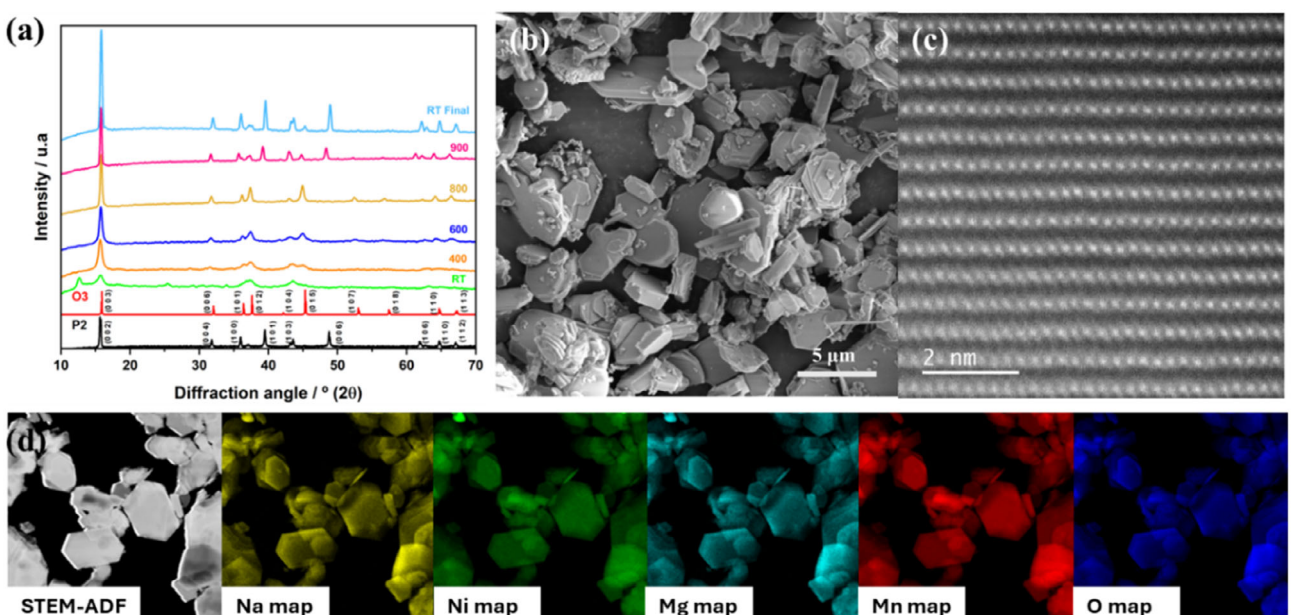


**Figure 5.** a) In situ XRD spectra of  $\text{Na}_{0.66}\text{Ni}_{0.27}\text{Mg}_{0.06}\text{Mn}_{0.66}\text{O}_2$  taken at room temperature (RT), 400, 600, 700, and 800 °C and after cooling back to room temperature inside the chamber (RT-Final) for the samples synthesized using the proposed organic route and the simulated pattern using a O3 (red) and P2 (black) structures. b) SEM micrograph of the synthesized particles and c) HR-STEM image of one of the  $\text{Na}_{0.66}\text{Ni}_{0.27}\text{Mg}_{0.06}\text{Mn}_{0.66}\text{O}_2$  particles along the [010] direction. d) ADF-STEM image and EDX elemental maps of Na, Ni, Mg, Mn, and O showing the elemental distribution within the  $\text{Na}_{0.66}\text{Ni}_{0.27}\text{Mg}_{0.06}\text{Mn}_{0.66}\text{O}_2$  particles.

Subsequently, the Na compound was electrochemically characterized. The synthesized samples have been cycled between 2 and 4.4 V (vs  $\text{Na}^+/\text{Na}$ ), for the first 100 cycles. Figure 6a shows the galvanostatic first charge/discharge curve of  $\text{Na}_{0.66}\text{Ni}_{0.27}\text{Mg}_{0.06}\text{Mn}_{0.66}\text{O}_2$  sample in sodium half cells. Additional charge–discharge curves corresponding to the 10th, 50th, and 100th cycles, and the corresponding  $dQ/dV$  curves can be found in (Figure S2, Supporting Information). In the galvanostatic charge/discharge profiles three plateaus at  $\approx 3.3$ ,  $\approx 3.7$ , and  $\approx 4.2$  V were observed during the first charge, with an initial charge capacity  $224 \text{ mA h g}^{-1}$  was observed, corresponding to the oxidation of  $\text{Ni}^{2+}$ . Figure 6b shows the CV curve 2–4.4 V potential window with scan rate of  $0.1 \text{ mV s}^{-1}$ . The sample exhibits anodic and cathodic bands attributable to the redox couples involved in the process during cycling. At lower voltages, the

redox couples located at 2.77/2.67 V correspond to the  $\text{Mn}^{4+}/\text{Mn}^{3+}$  redox process. Additionally, in the voltage range between 3 and 4 V, the cathode presents redox pairs that could be attributed to the  $\text{Ni}^{2+}/\text{Ni}^{3+}$  transition. A third contribution is observed at  $\approx 4.2$  V, which could be assigned to oxygen redox couples. These CV results are consistent with the plateaus in the corresponding galvanostatic curve. Figure 6c shows the capacity and capacity retention after 100 cycles.

The charge and discharge values ( $130$  and  $126 \text{ mA h g}^{-1}$ , respectively) and the coulombic efficiency (99%) and the rate performance are in good agreement with some of the best values reported in the bibliography for this compound.<sup>[31–34,54]</sup> Rate capability tests (Figure 6d) were performed cycling between 2 and 4.4 V vs  $\text{Na}^+/\text{Na}$  for kinetics from 0.5–10 C and returning to 0.5 C. The sample shows good capacity and capacity retention

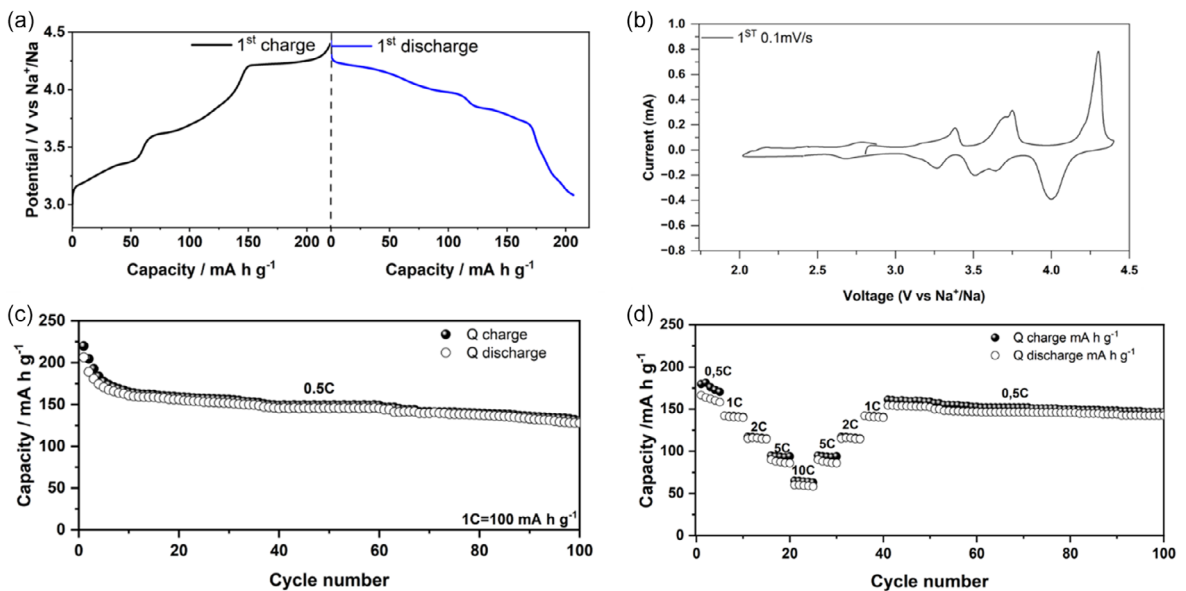


**Figure 6.** a) Galvanostatic first charge/discharge curve; b) CV curve of the  $\text{Na}_{0.66}\text{Ni}_{0.27}\text{Mg}_{0.06}\text{Mn}_{0.66}\text{O}_2$  sample, recorded using at a scan rate of  $0.1 \text{ mV s}^{-1}$ . c) Retention capacity profiles of the  $\text{Na}_{0.66}\text{Ni}_{0.27}\text{Mg}_{0.06}\text{Mn}_{0.66}\text{O}_2$  sample during the first 100 cycles. d) Rate performance of  $\text{Na}_{0.66}\text{Ni}_{0.27}\text{Mg}_{0.06}\text{Mn}_{0.66}\text{O}_2$  at room temperature.

even at high kinetics such as 10 C with a capacity of around  $50 \text{ mAh g}^{-1}$ . When the charge and discharge current densities are reduced from 10 to 0.5 C, ( $1 \text{ C} = 100 \text{ mA g}^{-1}$ ), the capacity can recover almost 100%.

For additional comparison, a sample of  $\text{Na}_{0.66}\text{Ni}_{0.27}\text{Mg}_{0.06}\text{Mn}_{0.66}\text{O}_2$  was synthesized using a conventional dry-milling method (see the Supporting Information for details about the synthesis and electrochemical characterization). In this case, the first charge capacity and the charge capacity after 100 cycles of the sample synthesized using the organic route are 51 and 65% higher, respectively (see Figure 4 and S4, Supporting Information), further validating the effectiveness of the proposed synthetic route.

As with the  $\text{Li}_{1.2}\text{Ni}_{0.2}\text{Mn}_{0.6}\text{O}_2$  sample, high-resolution STEM studies were conducted to investigate atomic-scale degradation mechanisms in  $\text{Na}_{0.66}\text{Ni}_{0.27}\text{Mg}_{0.06}\text{Mn}_{0.66}\text{O}_2$  particles. These mechanisms are associated with phase transitions driven by layer gliding, which, combined with volumetric changes due to sodium

(de)intercalation, lead to the formation of cracks within the particles. Additionally, surface restructuring occurs as a result of oxygen loss and interactions with the electrolyte.<sup>[55–59]</sup>

Figure 7 presents high-resolution STEM images of  $\text{Na}_{0.66}\text{Ni}_{0.27}\text{Mg}_{0.06}\text{Mn}_{0.66}\text{O}_2$  particles after one cycle and after 100 charge-discharge cycles. After the first cycle (Figure 7a), bending of the crystal planes due to interactions with the electrolyte is observed, along with the formation of a 6–8 nm-thick layer resulting from restructuring into rock-salt-type structures. After 100 cycles (Figure 7b), this layer grows to  $\approx 12\text{--}14 \text{ nm}$ , accompanied by increased amorphization at the particle surface.

This is consistent with the irreversible capacity loss seen after the first cycle and the progressive capacity fading over continued cycling, as bending, rock-salt, and amorphous structures hinder further sodium intercalation. However, it is noteworthy that in both cases, the layered structure is largely preserved in the bulk, which supports the high values of capacity measured.

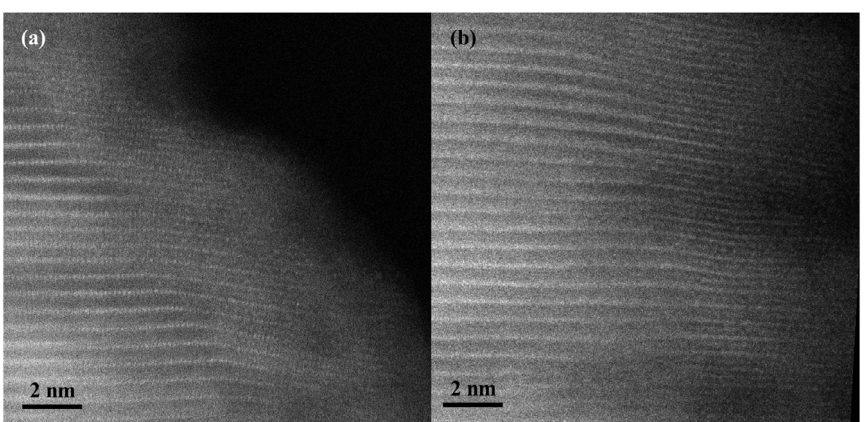


**Figure 7.** HR-STEM micrographs of particles a) after 1 charged-discharge cycle and b) after 100 cycles taken along the [100] direction.

### 3. Conclusion

In conclusion, this study demonstrates the successful fabrication of promising cathodes for Li-ion and Na-ion batteries, through a novel organic synthesis route that allows a drastic reduction of the synthesis times. This approach involves utilizing metal acetates and oleic acid to form an emulsion, which is subsequently heat-treated to yield the final product. Notably, the particles generated by this method exhibit shape, size, compositional homogeneity, and electrochemical behavior that closely resemble those obtained using the more conventional techniques. Remarkably, the particle size distribution achieved is highly similar to other techniques, such as sol-gel, recognized for providing excellent particle size uniformity, despite its time-consuming nature. The materials exhibit superior electrochemical properties that resemble some of the best results published so far in the literature. Furthermore, the proposed synthesis route uses organic precursors, producing reaction side-products that are noncontaminating, has a broad potential to be upscaled to an industrial level, and can be extended to the synthesis of other electrode materials.

## Experimental Section

### Synthesis of $\text{Li}_{1.2}\text{Ni}_{0.2}\text{Mn}_{0.6}\text{O}_2$

Stoichiometric amounts of  $\text{LiCOCH}_3$ ,  $\text{Ni}(\text{OCOCH}_3)_2 \cdot 4\text{H}_2\text{O}$  and  $\text{Mn}(\text{OCOCH}_3)_2 \cdot 4\text{H}_2\text{O}$ , from Sigma Aldrich, were mixed with 5 mL of distilled water, 10 mL of oleic acid, and 20 mL of Vaseline inside a Teflon container. The mixture was processed for 4 min using a shear mixer, in our case, a domestic hand-blender Taurus BAPI 750 INOX operating at 15,000 rpm. The resulting emulsion was poured into an alumina crucible and placed inside an oven with a heating ramp of  $5^\circ\text{C min}^{-1}$  with a target temperature of  $800^\circ\text{C}$ . It is worth noting that, during the heating ramp, at a temperature of  $\approx 100^\circ\text{C}$ , all the  $\text{H}_2\text{O}$  and  $\text{OH}^-$  groups are eliminated, and at  $\approx 450^\circ\text{C}$ , the calcination of the undesired organic groups will take place. Finally, once the temperature of  $800^\circ\text{C}$  is reached, the product is maintained inside the oven for 20 h and left to cool down to room temperature to achieve the  $\text{Li}_{1.2}\text{Ni}_{0.2}\text{Mn}_{0.6}\text{O}_2$  particles with the expected crystalline structure.

### Synthesis of $\text{Na}_{0.66}\text{Ni}_{0.27}\text{Mg}_{0.06}\text{Mn}_{0.66}\text{O}_2$

In this case, the metal acetates used were  $\text{Na}(\text{OCOCH}_3) \cdot 3\text{H}_2\text{O}$ ,  $\text{Mg}(\text{OCOCH}_3)_2 \cdot 4\text{H}_2\text{O}$ ,  $\text{Ni}(\text{OCOCH}_3)_2 \cdot 4\text{H}_2\text{O}$ , and  $\text{Mn}(\text{OCOCH}_3)_2 \cdot 4\text{H}_2\text{O}$ , also from Sigma Aldrich. The methodology to be followed is the same as in the case of  $\text{Li}_{1.2}\text{Ni}_{0.2}\text{Mn}_{0.6}\text{O}_2$ , with the only exception that the target temperature was  $900^\circ\text{C}$ , and the mixture was maintained for 10 h before cooling down to room temperature to obtain the  $\text{Na}_{0.66}\text{Ni}_{0.27}\text{Mg}_{0.06}\text{Mn}_{0.66}\text{O}_2$  particles.

### Characterization

The study of the crystallinity and the evolution of the crystal structure of the samples upon heating was performed by XRD in both in situ and ex situ spectrometers. The in situ experiments were carried out in a Bruker D8 Discover A25 diffractometer at different temperatures: room temperature (RT), 400, 600, 700, and  $800^\circ\text{C}$  (after being maintained at that temperature for 10 h), and after final cooling back to room temperature inside the furnace (RT Final).

To assess the morphology and average size of the synthesized particles, secondary-electron scanning electron microscopy (SE-SEM) experiments were carried out in a FEI Teneo SEM.

For the analysis of the nanostructure via TEM and related techniques, TEM samples were prepared by dispersing the particles in ethanol, followed by sonication, and drop casting on lacey carbon copper grids. STEM was performed using a FEI Talos F200S microscope operating at an accelerating voltage of 200 keV and equipped with a super-X energy-dispersive X-ray spectrometry (EDX) system, which includes four silicon drift detectors. The elemental mapping experiments were accomplished by combining annular dark-field imaging (ADF) and EDX acquisition in STEM mode. Further STEM analyses with atomic resolution were carried out on a FEI Titan Cubed Themis 60-300 and a JEOL ARM200F microscopes, both operating at 200 kV.

The electrochemical experiments on Li half-cells were carried out in Swagelock-type cells at ambient temperature. The cathode consisted of 80 wt% of active material, 10 wt% of carbon black, and 10 wt% of polyvinylidene fluoride (PVDF). The mixture was homogeneously dispersed into *N*-methyl pyrrolidine (NMP) and then spread onto Ti disks (Sigma-Aldrich, 99.7% purity and 0.127 mm thickness). To evaporate the NMP solvent, the electrode was dried for at least 2 h in a vacuum oven at  $120^\circ\text{C}$ . Glass fiber discs were used as separators. 1 M  $\text{LiPF}_6$  EC:DEC and lithium metal discs were used as the electrolyte and counter electrode, respectively. Swagelok-type cells were assembled in a glovebox under an argon atmosphere ( $\text{H}_2\text{O}, \text{O}_2 < 0.1 \text{ ppm}$ ). The cells were cycled between 4.8 and 2 V at  $50 \text{ mA g}^{-1}$ , and galvanostatic charge–discharge tests were conducted on an Ivium-n-Stat battery test system.

For Na half-cells, the electrochemical performance was measured by CR2023 coin cells at ambient temperature. The cathode slurry was prepared by hand grinding 70 wt% of active material, 20 wt% of carbon black (super P, MTI Corp), and 10 wt% of PVDF (MTI Corp) with NMP (Sigma-Aldrich). The slurry was cast on Al foil (MTI Corp) and dried at  $80^\circ\text{C}$  oven for at least 2 h and then punch into 12 mm-diameter electrode. The electrodes were further dried overnight at  $80^\circ\text{C}$  in a vacuum oven. The cells were assembled in a glovebox under an argon atmosphere ( $\text{H}_2\text{O}, \text{O}_2 < 0.1 \text{ ppm}$ ); 1 M sodium hexafluorophosphate ( $\text{NaPF}_6$ , Fluorochem, >98.0%) in propylene carbonate (PC, Sigma-Aldrich, anhydrous, 99.7%) with 5 vol% of fluoroethylene carbonate (FEC, Sigma-Aldrich, anhydrous, 99%), denoted as 1 M  $\text{NaPF}_6/\text{PC} + 5 \text{ vol\% FEC}$ , was applied as the electrolyte. The metallic Na chip (Sigma-Aldrich) was used as the counter/reference electrode, and a piece of glass fiber (Cytiva, GF/D) was used as the separator with  $100 \mu\text{L}$  of electrolyte injected. The cells were cycled between 4.4 and 2 V at  $50 \text{ mA g}^{-1}$ , and galvanostatic charge–discharge tests were conducted on a LAND battery testing system.

### Acknowledgements

Financial support was provided by the grant PID 2020-113108RB-I00 funded by MICIU/AEI/10.13039/501100011033 and, as appropriate, by "ERDF A way of making Europe," by "ERDF/EU," by the "European Union," or by the "European Union NextGenerationEU/PRTR." Financial support was also provided by the Grant CNS2022-135432 funded by MICIU/AEI/10.13039/501100011033 and, as appropriate, by "ESF Investing in your future," by "ESF+," or by "European Union NextGenerationEU/PRTR." The authors are also grateful to the Universidad de Sevilla for the use of the research facilities at CITIUS. The authors acknowledge the use of (S)TEM instrumentation provided by the National Facility ELECMIC ICTS ("División de Microscopía Electrónica," Universidad de Cádiz, DME-UCA) and the Advanced

Microscopy Laboratory at the Centre for Research on Adaptive Nanostructures and Nanodevices, Trinity College Dublin.

## Conflict of Interest

The authors declare no conflict of interest.

## Data Availability Statement

The data that support the findings of this study are available from the corresponding author upon reasonable request.

**Keywords:** batteries · cathodes · organic · shear mixer · synthesis method

- [1] J. Liu, Y. Wu, B. Zhang, X. Xiao, Q. Hu, Q. Han, L. Wang, F. Bei, X. He, *Small* **2024**, *20*, 2309629.
- [2] M. A. M. Alsamet, E. Burgaz, *Electrochim. Acta* **2021**, *367*, 137530.
- [3] L. Wang, B. Huang, W. Xiong, M. Tong, H. Li, S. Xiao, Q. Chen, Y. Li, J. Yang, *J. Alloys Compd.* **2020**, *844*, 156034.
- [4] Q. Jiang, L. Xu, J. Huo, H. Zhang, S. Wang, *RSC Adv.* **2015**, *5*, 75145.
- [5] J. H. Mugumya, M. L. Rasche, R. F. Rafferty, A. Patel, S. Mallick, M. Mou, J. A. Bobb, R. B. Gupta, M. Jiang, *Energy Fuels* **2022**, *36*, 12261.
- [6] Y. Shen, H. Xue, S. Wang, D. Zhang, D. Yin, L. Wang, Y. Cheng, *Chem. Eng. J.* **2021**, *411*, 128487.
- [7] H. Dong, G. M. Koenig, *CrystEngComm* **2020**, *22*, 1514.
- [8] C. Lin, Y. Zhang, L. Chen, Y. Lei, J. Ou, Y. Guo, H. Yuan, D. Xiao, *J. Power Sources* **2015**, *280*, 263.
- [9] W. B. Hua, X. D. Guo, Z. Zheng, Y. J. Wang, B. H. Zhong, B. Fang, J. Z. Wang, S. L. Chou, H. Liu, *J. Power Sources* **2015**, *275*, 200.
- [10] R. Zhao, Z. Yang, J. C. Chen, Z. Chen, J. Liang, H. Chen, *J. Alloys Compd.* **2015**, *627*, 206.
- [11] Y. Zhang, K. Du, Y. Cao, Y. Lu, Z. Peng, J. Fan, L. Li, Z. Xue, H. Su, G. Hu, *J. Power Sources* **2020**, *477*, 228701.
- [12] Y. Xiang, Y. Jiang, S. Liu, J. Wu, Z. Liu, L. Zhu, L. Xiong, Z. He, X. Wu, *Front. Chem.* **2020**, *8*, 00729.
- [13] D. V. Trinh, M. T. T. Nguyen, H. T. M. Dang, D. T. Dang, H. T. T. Le, H. T. N. Le, H. V. Tran, C. D. Huynh, *Sci. Rep.* **2021**, *11*, 12280.
- [14] W. He, X. Li, J. Chen, F. Peng, R. Zhang, Y. Liu, Z. Xiao, *Mater. Chem. Phys.* **2015**, *155*, 9.
- [15] J. A. K. Satrughna, A. R. Kanwade, S. M. Rajore, M. K. Tiwari, Y. Ito, A. Ogura, H. Lee, Y. Ohshita, P. M. Shirage, *Electrochim. Acta* **2024**, *507*, 145201.
- [16] J. Li, X. Wang, J. Zhao, J. Chen, T. Jia, C. Cao, *J. Power Sources* **2016**, *307*, 731.
- [17] J. Guo, W. Li, *ACS Appl. Energy Mater.* **2022**, *5*, 397.
- [18] U. Nisar, S. A. J. A. Al-Hail, P. R. Kumar, J. J. Abraham, S. M. A. Mesallam, R. A. Shakoor, R. Amin, R. Essehli, S. Al-Qaradawi, *Energy Technol.* **2021**, *9*, 2100085.
- [19] K. M. Shaju, P. G. Bruce, *Adv. Mater.* **2006**, *18*, 2330.
- [20] F. J. García-García, R. Klee, P. Lavela, M. R. D. Bomio, J. L. Tirado, *ChemElectroChem* **2020**, *7*, 3528.
- [21] B. H. Kim, Y. K. Choi, Y. H. Choa, *Solid State Ionics* **2003**, *158*, 281.
- [22] S.-T. Myung, S. Komaba, N. Kumagai, *J. Electrochem. Soc.* **2001**, *148*, A482.
- [23] K.-T. Hwang, W.-S. Um, H.-S. Lee, J.-K. Song, K.-W. Chung, *J. Power Sources* **1998**, *74*, 169.
- [24] T. H. Cho, H. T. Chung, *J. Appl. Electrochem.* **2005**, *35*, 1033.
- [25] T. Dong-Ge, L. Qiong-Yu, W. Ni-Ni, T. Ai-Dong, T. Lian-Xing, H. Ke-Long, J. Xiao-Yang, *Mater. Chem. Phys.* **2005**, *94*, 423.
- [26] M. A. Mudassir, S. Kousar, M. Ehsan, M. Usama, U. Sattar, M. Aleem, I. Naheed, O. Bin Saeed, M. Ahmad, H. F. Akbar, M. A. Ud Din, T. M. Ansari, H. Zhang, I. Hussain, *Renewable Sustainable Energy Rev.* **2023**, *185*, 113594.
- [27] A. H. Marincaş, F. Goga, S. A. Dorneanu, P. Illea, *J. Solid State Electrochem.* **2020**, *24*, 473.
- [28] Y. Tian, G. Zeng, A. Rutt, T. Shi, H. Kim, J. Wang, J. Koettgen, Y. Sun, B. Ouyang, T. Chen, Z. Lun, Z. Rong, K. Persson, G. Ceder, *Chem. Rev.* **2021**, *121*, 1623.
- [29] M. Malik, K. H. Chan, G. Azimi, *Mater. Today Energy* **2022**, *28*, 101066.
- [30] S.-T. Myung, S. Komaba, N. Kumagai, H. Yashiro, H.-T. Chung, T.-H. Cho, *Electrochim. Acta* **2002**, *47*, 2543.
- [31] C. Cheng, H. Hu, C. Yuan, X. Xia, J. Mao, K. Dai, L. Zhang, *Energy Storage Mater.* **2022**, *52*, 10.
- [32] C. Shi, L. Wang, X. Chen, J. Li, S. Wang, J. Wang, H. Jin, *Nanoscale Horiz.* **2021**, *7*, 338.
- [33] K. Wang, H. Wan, P. Yan, X. Chen, J. Fu, Z. Liu, H. Deng, F. Gao, M. Sui, *Adv. Mater.* **2019**, *31*, 1904816.
- [34] Q. Mao, Y. Yu, J. Wang, L. Zheng, Z. Wang, Y. Qiu, Y. Hao, X. Liu, *J. Mater. Chem. A Mater.* **2021**, *9*, 10803.
- [35] I. Hasa, D. Buchholz, S. Passerini, J. Hassoun, *ACS Appl. Mater. Interfaces* **2015**, *7*, 5206.
- [36] K. Redel, A. Kulka, K. Walczak, A. Plewa, E. Hanc, M. Marzec, L. Lu, J. Molenda, *Chem. Eng. J.* **2021**, *424*, 130293.
- [37] G. Assat, D. Foix, C. Delacourt, A. Iadecola, R. Dedryvère, J. M. Tarascon, *Nat. Commun.* **2017**, *8*, 2219.
- [38] K. Luo, M. R. Roberts, R. Hao, N. Guerrini, E. Liberti, C. S. Allen, A. I. Kirkland, P. G. Bruce, *Nano Lett.* **2016**, *16*, 7503.
- [39] K. Luo, M. R. Roberts, R. Hao, N. Guerrini, D. M. Pickup, Y. S. Liu, K. Edström, J. Guo, A. V. Chadwick, L. C. Duda, P. G. Bruce, *Nat. Chem.* **2016**, *8*, 684.
- [40] R. A. House, U. Maitra, L. Jin, J. G. Lozano, J. W. Somerville, N. H. Rees, A. J. Naylor, L. C. Duda, F. Massel, A. V. Chadwick, S. Ramos, D. M. Pickup, D. E. McNally, X. Lu, T. Schmitt, M. R. Roberts, P. G. Bruce, *Chem. Mater.* **2019**, *31*, 3293.
- [41] E. Boivin, N. Guerrini, R. A. House, J. G. Lozano, L. Jin, G. J. Rees, J. W. Somerville, C. Kuss, M. R. Roberts, P. G. Bruce, *Adv. Funct. Mater.* **2021**, *31*, 2003660.
- [42] J. Zhou, X. Zhou, W. Yu, Z. Shang, S. Xu, *Electrochim. Energy Rev.* **2024**, *7*, 13.
- [43] S. Karimzadeh, B. Safaei, C. Yuan, T. C. Jen, *Electrochim. Energy Rev.* **2023**, *6*, 24.
- [44] Y. Zhang, W. Zhang, M. Li, Z. Yang, G. Chen, Q. Wang, *J. Mater. Chem. A Mater.* **2013**, *1*, 14368.
- [45] A. Pan, D. Choi, J. G. Zhang, S. Liang, G. Cao, Z. Nie, B. W. Arey, J. Liu, *J. Power Sources* **2011**, *196*, 3646.
- [46] A. K. Shukla, Q. M. Ramasse, C. Ophus, H. Duncan, F. Hage, G. Chen, *Nat. Commun.* **2015**, *6*, 8711.
- [47] J. Zhang, H. Zhang, R. Gao, Z. Li, Z. Hu, X. Liu, *Phys. Chem. Chem. Phys.* **2016**, *18*, 13322.
- [48] E. Wang, C. Shao, S. Qiu, H. Chu, Y. Zou, C. Xiang, F. Xu, L. Sun, *RSC Adv.* **2017**, *7*, 1561.
- [49] Y. Puheng, W. Wenwu, Z. Xiaoliang, L. Honglei, Z. Shichao, X. Yalan, *RSC Adv.* **2018**, *8*, 39769.
- [50] J. Hong, D. H. Seo, S. W. Kim, H. Gwon, S. T. Oh, K. Kang, *J. Mater. Chem.* **2010**, *20*, 10179.
- [51] J. G. Lozano, G. T. Martinez, L. Jin, P. D. Nellist, P. G. Bruce, *Nano Lett.* **2018**, *18*, 6850.
- [52] J. Zheng, P. Xu, M. Gu, J. Xiao, N. D. Browning, P. Yan, C. Wang, J. G. Zhang, *Chem. Mater.* **2015**, *27*, 1381.
- [53] D. Mohanty, A. S. Sefat, S. Kalnaus, J. Li, R. A. Meissner, E. Andrew Payzant, D. P. Abraham, D. L. Wood, C. Daniel, *J. Mater. Chem. A Mater.* **2013**, *1*, 6249.
- [54] N. Yabuuchi, R. Hara, M. Kajiyama, K. Kubota, T. Ishigaki, A. Hoshikawa, S. Komaba, *Adv. Energy Mater.* **2014**, *4*, 1301453.
- [55] U. Maitra, R. A. House, J. W. Somerville, N. Tapia-Ruiz, J. G. Lozano, N. Guerrini, R. Hao, K. Luo, L. Jin, M. A. Pérez-Osorio, F. Massel, D. M. Pickup, S. Ramos, X. Lu, D. E. McNally, A. V. Chadwick, F. Giustino, T. Schmitt, L. C. Duda, M. R. Roberts, P. G. Bruce, *Nat. Chem.* **2018**, *10*, 288.
- [56] T. Y. Yu, H. H. Ryu, G. Han, Y. K. Sun, *Adv. Energy Mater.* **2020**, *10*, 2001609.
- [57] S. Xu, L. Zhao, S. Li, S. Guo, *Chem. Commun.* **2025**, *61*, 4147.
- [58] T. Jin, P. F. Wang, Q. C. Wang, K. Zhu, T. Deng, J. Zhang, W. Zhang, X. Q. Yang, L. Jiao, C. Wang, *Angew. Chem. - Int. Ed.* **2020**, *59*, 14511.
- [59] P. Yan, J. Zheng, M. Gu, J. Xiao, J. G. Zhang, C. M. Wang, *Nat. Commun.* **2017**, *8*, 14101.

Manuscript received: March 22, 2025

Revised manuscript received: April 24, 2025

Version of record online: